

# MSDiff: Multi-Scale Diffusion Model for Ultra-Sparse View CT Reconstruction

Pinhuang Tan, Mengxiao Geng, Jingya Lu, Liu Shi, Bin Huang, Qiegen Liu, *Senior Member, IEEE*

**Abstract**—Computed Tomography (CT) technology reduces radiation hazards to the human body through sparse sampling, but fewer sampling angles pose challenges for image reconstruction. Score-based generative models are widely used in sparse-view CT reconstruction, performance diminishes significantly with a sharp reduction in projection angles. Therefore, we propose an ultra-sparse view CT reconstruction method utilizing multi-scale diffusion models (MSDiff), designed to concentrate on the global distribution of information and facilitate the reconstruction of sparse views with local image characteristics. Specifically, the proposed model ingeniously integrates information from both comprehensive sampling and selectively sparse sampling techniques. Through precise adjustments in diffusion model, it is capable of extracting diverse noise distribution, furthering the understanding of the overall structure of images, and aiding the fully sampled model in recovering image information more effectively. By leveraging the inherent correlations within the projection data, we have designed an equidistant mask, enabling the model to focus its attention more effectively. Experimental results demonstrated that the multi-scale model approach significantly improved the quality of image reconstruction under ultra-sparse angles, with good generalization across various datasets.

**Index Terms**—Computed tomography, multi-diffusion model, ultra-sparse view reconstruction, sinogram domain.

## I. INTRODUCTION

Computed tomography (CT) utilizes X-ray to achieve tomographic imaging of the human body, providing crucial three-dimensional internal structural information. It plays an indispensable role in clinical diagnosis [1], [2]. However, statistics show that up to 60% of CT examinations use an excessively high radiation dose [3], which may significantly increase patient cancer risks [4]. Currently, one of the main methods to reduce radiation dosage is to decrease the number of projection angles [5]. There are generally two strategies to reduce projection an-

gles: one is to conduct projections over the 360° range but increase the interval between projection angles, known as sparse-angle reconstruction, the other is continuous projection over a range less than 180°, referred to as limited-angle reconstruction. To mitigate the impact of radiation exposure from CT scans on patients, the sparse-angle CT reconstruction approach has been extensively adopted. Nevertheless, there remain issues with such methods. Due to the limited number of acquired angles, the obtained projection data is incomplete, leading to poor reconstruction quality and pronounced artifacts and distortions using filtered back projection (FBP) algorithms [6], [7], [8]. Niu *et al.* compared with FBP reconstruction results under different view angles. The results showed obvious pseudo-artifacts when view angles were reduced to 60° [9]; Wang *et al.* also pointed out traditional FBP algorithms require complete view data and perform poorly with sparse views [10]. How to effectively resolve these problems while maintaining image quality is of great significance for clinical medical imaging.

To effectively reduce CT radiation dosage, researchers have explored various algorithms to reconstruct full-view CT images from sparse-view data. Sidky *et al.* [11], [12] introduced compressive sensing (CS) theory into CT reconstruction, representing prior information with regularization methods to solve many ill posed inverse problems. Chen *et al.* [13] proposed a limited-angle CT reconstruction method based on anisotropic TV minimization, which can reconstruct full-view CT images from sparse-angle CT data by leveraging prior knowledge and mathematical optimization. Xi *et al.* [14] presented an adaptive-weighted higher-order total variation algorithm to address pseudo artifacts in sparse-data filtered back projection. In the field of deep learning, Ma *et al.* [15] designed a FreeSeed network for sparse-view CT reconstruction. Lee *et al.* [16] synthesized complete sinusoidal graphs with deep neural networks to reconstruct full-view CT. Zhang *et al.* [17] built a DREAM-Net, leveraging projection completion, residual learning and other modules collaboratively for full-view CT reconstruction. However, the commonly used sparse-view CT acquisition pattern today typically requires scanning and collecting projection data from 20-60 view angles [18], [19]. Although radiation dose is reduced by 50%-80% compared to full-view CT scanning, such levels remain too high for certain vulnerable groups with potential hazards [20], [21]. Moreover, scanning 20-60 views takes time, unfriendly to emergency patients needing rapid diagnosis [22]. Consequently, by reducing the CT view angles to 10 or fewer, significantly reducing radiation exposure and scanning time for patients. This approach renders the technology more suitable for vulnerable groups and emergency cases.

Ultra-sparse view uses even fewer X-ray projection view angles to acquire data, typically only one-tenth to one-fifth of ordi-

This work was supported in part by National Natural Science Foundation of China under 62122033 and Key Research and Development Program of Jiangxi Province under 20212BBE53001. (P. Tan and M. Geng are co-first authors.) (Corresponding authors: B. Huang and Q. Liu)

P. Tan, M. Geng, and Q. Liu are with the School of Information Engineering, Nanchang University, Nanchang 330031, China. ({tanpinhuang, mxiaogeng, liuyi}@email.ncu.edu.cn, liuqiegen@ncu.edu.cn)

J. Lu is with the School of Nursing, Nanchang University, Nanchang 330031, China. (e-mail: x993631231@gmail.com)

B. Huang, is with School of Mathematics and Computer Sciences, Nanchang University, Nanchang 330031, China. (huangbin@email.ncu.edu.cn)

Liu Shi is with the Beijing Engineering Research Center of Radiographic Techniques and Equipment, Institute of High Energy Physics, Chinese Academy of Sciences, Beijing 100049, China, and also with the School of Nuclear Science and Technology, University of Chinese Academy of Sciences, Beijing 100049, China. (e-mail: shiliu@ihep.ac.cn)

nary sparse view. Adopting ultra-sparse view can tremendously reduce CT radiation dose, better achieving the ALARA principle and alleviating radiation harm to patients [23]. However, ultra-sparse view leads to severe stripe pseudo-artifacts in the reconstructed images. To address this, Wu *et al.* proposed DOSM, incorporating data consistency into SDE for ultra-sparse-view CT reconstruction, achieving excellent performance with minimal views [24]. Chan *et al.* proposed an end-to-end attention-based network, first reconstructing with FBP and then removing artifacts [25]. Although some progress has been made, the image quality still hardly meets diagnostic needs. How to obtain acceptable diagnostic CT images under ultra-low radiation dose remains a significant challenge. Recently, Saharia *et al.* proposed an iterative refinement-based diffusion model for image super-resolution, demonstrating the potential of diffusion models in image reconstruction tasks [26]. Although not directly applied to CT reconstruction, their work suggests that diffusion models can effectively enhance image quality in various reconstruction scenarios. Guan *et al.* adopted a fully unsupervised score-based generative model for sparse-view CT reconstruction, showing it can achieve quality comparable to supervised adversarial learning [27]. This proves diffusion models can conduct high-quality image reconstruction without requiring complete paired training data. Additionally, Xu *et al.* applied diffusion models to progressively reconstruct sparse-view CT in the wavelet domain, also achieving remarkable improvement in image quality [28]. Michael *et al.* [29] explored applications of score-based diffusion models in Bayesian image reconstruction, using diffusion models for various reconstruction tasks. Wang *et al.* [30] proposed a sub-volume-based 3D denoising diffusion probabilistic model (DDPM) for CBCT image reconstruction from sparsely-sampled data. Xia *et al.* [31] presented a patch-based DDPM for sparse-view X-ray computed tomography reconstruction. Li *et al.* [32] introduced a framework named DDMM-Synth combining diffusion models with CT measurement embedding inverse sampling schemes for sparse CT reconstruction. Huang *et al.* [33] proposed a projection-domain fully unsupervised single-sample diffusion model (OSDM) for low-dose CT reconstruction, which takes abundant tensors extracted from the structure-Hankel matrix as network input to capture prior distribution. These further prove the efficacy of diffusion models in suppressing noise and restoring details by controlling random processes, enabling high-quality reconstruction for sparse-view CT.

Despite the relative success achieved by existing diffusion models in sparse CT image reconstruction, ultra-sparse CT image reconstruction poses challenges due to the lack of sufficient projection data. This may lead to issues such as decreased resolution and artifacts, ultimately affecting the quality and accuracy of reconstructed images. To address this issue, this study proposes a multi-scale diffusion model for ultra-sparse view CT reconstruction. This method involves alternating iterative reconstruction using multiple diffusion models with diverse prior distribution, aiming to significantly enhance the quality of CT images reconstructed from highly sparse views. In summary, the main contributions of this work can be summarized as follows:

- We propose a reconstruction method for a multi-scale diffusion model to enhance the restoration of local textures and details. Due to the extremely limited information contained in the ultra-sparse views, our method aims to fully utilize existing data and integrate the extraction of local projection infor-

mation by the model to compensate for the challenges caused by data missing. Integrating local projection with structural details enhances both the accuracy of image reconstruction and the restoration of local details, while ensuring global consistency.

- We employ the existing correlation in projection data to design specialized masks for extracting sparse priors. This method utilizes fewer prior cues, thereby enhancing the comprehension of the model for sparse data distribution. At the same time, the model can more precisely capture crucial features within the data, thus facilitating a more accurate restoration of local textures and details during the reconstruction process.

The structure of this work is arranged as follows: Section II provides a brief introduction to the relevant knowledge of CT reconstruction. Section III elaborates on the theory and algorithms of CT ultra-sparse projection reconstruction based on multiple diffusion models. Section IV showcases the experimental results and evaluations under ultra-sparse angle conditions. Section V discusses related issues. Finally, this work is summarized in Section VI.

## II. PREPARATION

### A. CT Reconstruction Model

CT image reconstruction starts with acquiring projection data, mathematically represented by the forward projection equation:

$$x = AI, \quad (1)$$

where  $x$  represents the vector of measured projection data, and  $A$  symbolizes the system matrix, which encompasses the physics of the CT imaging process. The system matrix  $A$  models the line integrals through the attenuation coefficients that are associated with the subject, which are discretely represented by the vector  $I$ . Thus, the product  $AI$  effectively simulates the projection data as if derived from the actual object.

To reconstruct images from projections, the optimization problem is solved as follows:

$$\min_I \{\|AI - x\|_2^2 + \lambda R(I)\}, \quad (2)$$

where  $\|AI - x\|_2^2$  is the data fidelity term and  $R(I)$  is the regularization term to describe prior knowledge of the image.  $\lambda$  is a positive parameter used to balance these terms.

The transition from full projection data to sparse-view data can be interpreted as a linear measurement process. Fig. 1 provides an intuitive visualization of this linear measurement process. By applying the Radon transform  $r$ , the original image is transformed into the projection data. Additionally,  $m$  represents the subsampling mask for the projection data, and  $P(m)$  subsamples the sinogram to sparse-view data with subsampling mask. Consequently, the sparse-view CT reconstruction problem can be formulated as:

$$y = P(m)AI = P(m)x, \quad (3)$$

where  $y$  is the sparse-view CT projection data and  $x$  represents the full-view projection data.

In scenarios involving sparse-view projection, strip artifacts are commonly produced when images are reconstructed directly using the FBP algorithm. For the acquisition of higher quality reconstructed images, full-view projection data must be derived from sparse-view projection data, a process that constitutes an

underdetermined inverse problem. To address this problem, various priors are incorporated into a regularized objective function, which is expressed as follows:

$$x = \underset{x}{\operatorname{argmin}}\{\|P(m)x - y\|_2^2 + \lambda R(x)\}. \quad (4)$$

The objective function consists of two terms. The first term represents the data fidelity, ensuring that the sparse-view sinogram aligns with the estimated measurements obtained through the subsampling mask. The second term is the regularization term, where  $\lambda$  helps maintain an appropriate balance between data fidelity and regularization term.

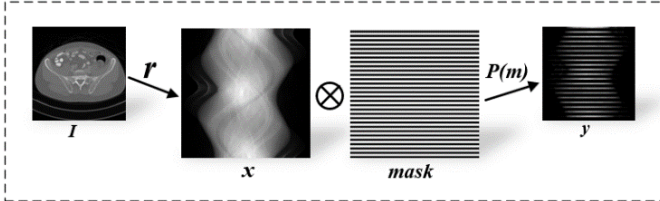


Fig. 1. Linear measurement process for sparse-view CT.

### B. Diffusion Model

In recent years, deep generative models based on diffusion processes have shown great potential in modeling complex high-dimensional data distribution [34], [35]. Diffusion-based models can be categorized into two main types:

**Denoising Diffusion Probabilistic Models (DDPMs):** Sohl-Dickstein *et al.* first proposed learning the reverse diffusion process to infer data distribution [36], which inspired DDPMs. A typical example is DDPMs proposed by Ho *et al.* [37], which learns distribution by simulating the reverse diffusion of data generation processes. DDPMs use Gaussian noise and assumes a Markov diffusion process. Researchers have made various improvements to DDPMs, including using non-Markovian processes [38], mixed Gaussian noise [39], forming models like the denoising diffusion implicit model (DDIM). These DDPMs demonstrate strong ability in detail recovery and noise control.

**Score-based Models with Stochastic Differential Equations (SDEs):** Song *et al.* [40] introduced SDEs with forward and reverse-time SDEs into diffusion models. SDEs provide a mathematical framework to derive the score function. Models based on SDEs like Song *et al.* [41] and Wang *et al.* [42] have shown promising results. Compared to networks such as generative adversarial networks (GANs), diffusion-based models can better capture complex data structures [43]. They pioneer a new paradigm for learning complex distribution.

## III. METHOD

### A. Motivation

CT projection data are typically represented in graphs, containing complex features and structural information of projection images. Sparse projection data, acquired from limited angles, are designated as such. Compared to complete projection data, sparse projection data are found to be more sensitive to noise. While traditional reconstruction algorithms can be effective under certain conditions, a diminishment in performance is observed with reduced projection angles, especially in ultra-sparse views. Streaking and aliasing artifacts may be produced during the reconstruction of ultra-sparse projection data, posing signifi-

cant challenges in ultra-sparse view scenarios. In this study, a novel model for reconstructing ultra-sparse views is proposed to enhance the overall visual quality of images. Specifically, two diffusion models, the Full-view Diffusion Model (FDM) and the Sparse-view Diffusion Model (SDM), are trained to extract global and specific local information from fully sampled and sparsely projected data, respectively. By leveraging the respective strengths of these models, the approximation of the ideal image is aimed. More precisely, the overall characteristics of the projection data are effectively captured by the FDM, which also reduces noise and artifacts. The reconstruction process is assisted by the SDM, which complements the FDM by highlighting intrinsic connections between structures and demonstrating unique advantages in structures, edges, textures, and other aspects. By integrating multiple diffusion models to mutually constrain each other, the stability of ultra-sparse view CT reconstruction is significantly enhanced. The reconstruction of ultra-sparse view is achieved by iteratively processing specific sparse projection data, as illustrated in Fig. 2. From left to right, sparse projection data are sequentially reconstructed to approximate the ground truth (GT).

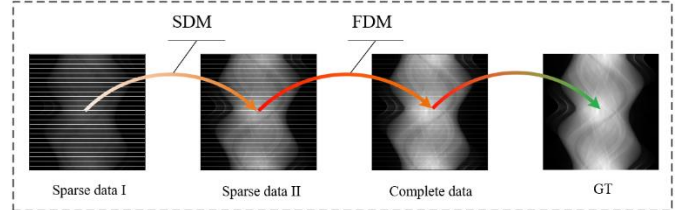


Fig. 2. The proposed reconstruction scheme integrates both global and local information. SDM represents targeted reconstruction for specific subsets of data. FDM represents global information reconstruction for various image features. GT represents ideal projection data.

### B. Prior Learning in Projection Domain

During the model training process, the SDM and the FDM are trained separately using masked sparsely-sampled sinogram data along with completely fully-sampled data. To simplify and accelerate the explanation, the shorthand notation  $x_1$  is introduced for full-view projection data, and  $x_2$  for sparse-view projection data. The specific masking operator is defined as follows:

$$x_1 = x, \quad (5)$$

$$x_2 = x \odot \text{mask}_1, \quad (6)$$

where  $\text{mask}_1$  is the specific mask matrix operator used to separate the information for training.  $x$  represents input fully-sampled projection data.  $\odot$  represents element-wise multiplication. At specific sparse sampling angles, row matrices assigned for partial information extraction are assigned a value of 1, whereas other areas are marked with a value of 0. Therefore, areas falling outside the designated sparse sampling angles are ignored, allowing the algorithm to focus solely on data captured at positions marked with 1. These positions, identified by row matrices valued at 1, are recognized as sampling points under consideration, facilitating the preservation of potential structural information within the image. Conversely, areas marked with a value of 0 are disregarded, which aids in reducing noise introduction. This approach effectively reduces the volume of data and assists the model in concentrating on learning and reconstructing fundamental data characteristics.

The utilization of the SDE model to learn the statistical distribution characteristics of CT sinogram data is illustrated in Fig. 3. Fig. 3(a) illustrates the diffusion process in the projection domain, where both FDM and SDM follow the same process. Sparse projection data from 120 views are used to train the SDM in Fig. 3(b).  $S_{\theta_1}$  and  $S_{\theta_2}$  respectively denote the training score networks associated with FDM and SDM. Specifically, Gaussian noise is continuously added to the images, and through the encoder and decoder, a transition is gradually made from a coarse prior distribution to an accurate posterior distribution, thereby enabling the generation of clear reconstructed images.

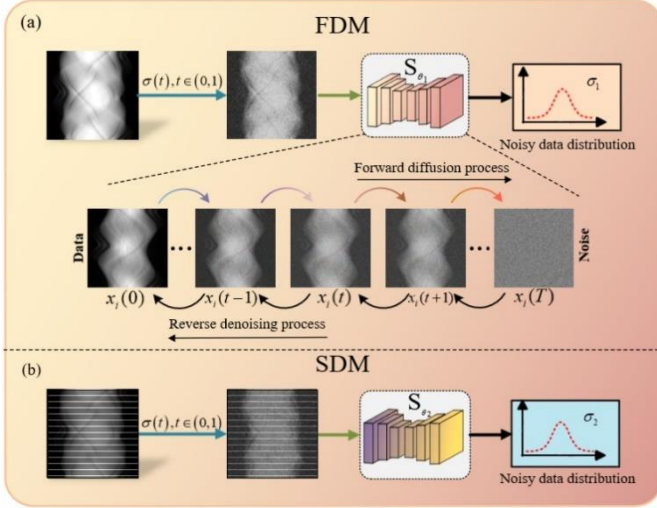


**Fig. 3.** Visualization of the diffusion process of MSDiff in the projection domain. From top to bottom: (a) Detailed training procedure of FDM, including the forward diffusion and reverse diffusion processes. (b) Detailed training procedure of SDM.

The original fully-sampled sinogram data and sparsely-sampled sinogram data are used as inputs to simulate the forward diffusion process of the Stochastic Differential Equation (SDE) [38], allowing the model to gradually approximate the actual distribution of different sinogram data. The diffusion processes for the two models can be represented by the following formula:

$$dx = f(x, t)dt + g(t)d\mathbf{w}, \quad (7)$$

where  $f(x, t) \in \mathbb{R}^n$  represents the drift coefficient, and  $g(t)$  denotes the diffusion coefficient. The term  $\mathbf{w} \in \mathbb{R}^n$  introduces Brownian motion.

To be specific, the variance exploding (VE)-SDE configuration ( $f(x, t) = 0, g(t) = \sqrt{d[\sigma^2(t)]/dt}$ ) is embraced, a choice that imparts heightened generative prowess. Upon the incorporation of  $x_1$  and  $x_2$  into (7), the equation metamorphoses into the following forms:

$$dx_1 = \sqrt{d[\sigma_1^2(t)]/dt} d\mathbf{w}, \quad (8)$$

$$dx_2 = \sqrt{d[\sigma_2^2(t)]/dt} d\mathbf{w}, \quad (9)$$

where  $\sigma(t) > 0$  is represented as a monotonically increasing function. It is thoughtfully chosen to manifest as a geometric series. Samples of  $x(T) \sim P_T$  are started from, and through the reversal of the process, samples  $x(0) \sim P_0$  are obtained. It is a recognized principle in stochastic calculus that the reverse process of diffusion retains the characteristics of diffusion. Thus, the following reverse-time SDE is obtained:

$$\begin{aligned} dx &= [f(x, t) - g^2(t)\nabla_x \log p_t(x)]dt + g(t)d\mathbf{w} \\ &= \frac{d[\sigma^2(t)]}{dt} \nabla_x \log p_t(x) + \sqrt{\frac{d[\sigma^2(t)]}{dt}} d\mathbf{w}, \end{aligned} \quad (10)$$

In this work, all score functions are estimated using a time-conditioned neural network. Although the true scores are not directly known, it is assumed that  $x(0)$  follows the initial data distribution of the projection views  $p_0$ , and  $x(T)$  conforms to the prior distribution  $p_t$ . To substitute for the unknown  $\nabla_x \log p_t(x)$ , a denoising score matching technique is employed, where  $\nabla_x \log p_t(x|x(0))$  represents data centered around a Gaussian perturbation kernel at  $x(0)$ . Under certain regularization conditions, as specified in (10), the score function  $S_\theta(x, t)$  trained with denoising score matching is nearly certain to satisfy the target function  $S_\theta(x, t) \approx \nabla_x \log p_t(x)$ . Through systematic training of the neural network  $S_\theta$ , the calculation of score functions is approximated, thereby capturing the essence of  $\nabla_x \log p_t(x)$ , which is represented as  $S_\theta(x, t) = \nabla_x \log p_t(x(t))$ . By training the score network to obtain the data distribution  $S_\theta = \{S_{\theta_1}, S_{\theta_2}\}$ , it is inserted into (10) and the resulting reverse-time SDE is solved for reconstruction.

$$dx = [f(x, t) - g^2(t)S_\theta(x, t)]dt + g(t)d\mathbf{w}. \quad (11)$$

Furthermore, it is necessary to fine-tune the neural network's parameters  $\theta^*$ , to accurately estimate  $\nabla_x \log p_t(x)$ . This process is considered the core objective function of a score-based Stochastic Differential Equation (SDE):

$$\begin{aligned} \theta^* &= \operatorname{argmin}_{\theta} \{ \lambda(t) \mathbb{E}_{x(0)} \mathbb{E}_{x(t)|x(0)} [ \| S_\theta(x(t), t) \\ &\quad - \nabla_{x(t)} \log p_t(x(t)|x(0)) \|_2^2 ] \}, \end{aligned} \quad (12)$$

where,  $\lambda(t)$  represents a positively weighted function, and  $t$  is uniformly sampled from the interval  $[0, T-1]$ . The term  $p_t(x(t)|x(0))$  signifies the Gaussian perturbation kernel centered around  $x(0)$ . A neural network  $S_\theta$  is systematically trained to approximate the score, allowing it to capture the essence of  $\nabla_x \log p_t(x)$ , *i.e.*,  $S_\theta = \nabla_x \log p_t(x)$ . Upon achieving full model proficiency, the value of  $\nabla_x \log p_t(x)$  can be effectively determined across all time points  $t$  through the solution of  $S_\theta(x(t), t)$ . This equips the model with an ample reservoir of prior knowledge, thereby enabling it to skillfully undertake the process of image reconstruction.

Learning the distribution of specific sparse projection data enables the extraction of relevant structural information. Coupled with the comprehensive generation capability of the full-view projection model, this enhances the adaptability and generalization ability of the model to data with different sampling rates. Therefore, the low-sampling-rate training strategy improves the modeling and reconstruction ability of the model for sparse-view data to some extent, which is an effective method to enhance the reconstruction quality. **Algorithm 1** outlines the training process: training both the full-view projection model and the specific sparse-view projection model to capture prior distribution.

---

#### Algorithm 1: MSDiff for Training Process

---

- 1: Generating projection  $x$
  - 2: Under sampling:  $x_1 = x$ ,  $x_2 = x \odot \text{mask}_1$
  - 3: Training datasets distribution:  $x_1$  and  $x_2$
  - 4: Training with (12)
  - 5: Output:  $S_{\theta_1}(x_1, t)$  and  $S_{\theta_2}(x_2, t)$
-

### C. MSDiff: Iterative Reconstruction

This section describes the iterative reconstruction process of MSDiff. Fig. 4 intuitively displays a two-stage iterative method that combines the FDM and the SDM for image reconstruction. Initially, the ultra-sparse view sinogram  $U$  obtained from the CT device is interpolated using bilinear interpolation to achieve a preliminarily restored full-view sinogram  $x$ .

$$x = K(U), \quad (13)$$

where  $K$  represents a bilinear interpolation operation. Initial reconstruction for ultra-sparse projection data is conducted using SDM, with the sampling scheme determined by the sparse prior of SDM. Consequently, the full-view sinogram is element-wise multiplied by the corresponding *mask* to produce sparse-view images for SDM reconstruction. The overall framework of the iterative reconstruction process is described as follows:

$$\begin{cases} x'_{i-1,j} = \text{SDM}(x_{i,j} \odot \text{mask}_1), \\ x_{i-1,j} = x'_{i-1,j} + (1 - \text{mask}_1) \odot x_{i,j}, \\ x_{i-1,j-1} = \text{FDM}(x_{i-1,j}), \end{cases} \quad (14)$$

where  $i$  and  $j$  denote the total number of reverse iterations.  $x_{i-1,j-1}$  and  $x'_{i-1,j}$  represent the output results of networks utilizing different prior information corresponding to FDM and SDM, respectively. Since the SDM has been trained on the characteristic distribution of specific data, a limited yet precise amount of prior knowledge is provided to guide the reconstruction process, thereby effectively restoring the structural information and texture features within the sinogram data.

Subsequently, the reconstructed sparse views are superimposed with the sparse views reconstructed by SDM, resulting in the full-view sinogram  $x_{i-1,j}$ . Thereafter, the sinograms aligned through iterative reconstruction using FDM gradually restore richer details until convergence is achieved, yielding sinograms that closely approximate the original input. Upon completion of the MSDiff iterations, by integrating processing results from multiple scale levels, the MSDiff model produces the final reconstructed result. Eventually, the reconstructed image is obtained using the FBP algorithm. The expression is as follows:

$$\bar{I} = \text{FBP}(x), \quad (15)$$

where  $\bar{I}$  stands as the final reconstruction results produced by MSDiff method. It is noteworthy that the predictor-corrector (PC) sampler step is utilized in the model. This work introduces PC sampling at the samples updating step, as suggested in [44]. The predictor is viewed as a numerical solver for the reverse-time SDE in the PC sampling. Once the reverse-time SDE process concludes, samples are generated based on the discretized prior distribution, which can be discretized as follows:

$$x_k \leftarrow x_{k+1} + (\sigma_{k+1}^2 - \sigma_k^2)S_\theta(x_{k+1}, \sigma_{k+1}) + \sqrt{\sigma_{k+1}^2 - \sigma_k^2}z$$

$$k = T - 1, \dots, 0. \quad (16)$$

Where  $z \sim \mathcal{N}(0,1)$  refers to a standard normal distribution,  $x(0) \sim p_0$ , and  $\sigma_0 = 0$  is chosen to simplify the notation. The above formulation is repeated for  $k = T - 1, \dots, 0$ . During the reconstruction process of MSDiff,  $k$  is represented by either  $i$  or  $j$ . When it comes to the corrector, it refers to the Langevin dynamics via transforming any initial sample  $x(t)$  to the final sample  $x(0)$  with the following procedure:

$$x_{k,l} = x_{k,l-1} + \varepsilon_k S_\theta(x_{k,l-1}, \sigma_k) + \sqrt{2\varepsilon_k}z$$

$$l = 1, 2, \dots, M, k = T - 1, \dots, 0. \quad (17)$$

where  $\varepsilon_k > 0$  is the step size, and the above equation is repeated for  $l = 1, 2, \dots, M, k = T - 1, \dots, 0$ . The theory of Langevin dynamics guarantees that when  $M \rightarrow 0$  and  $\varepsilon_k \rightarrow 0$ ,  $x_k$  is sampled from  $p_t(x)$  under designated conditions.

Moreover, to ensure that the output remains consistent with the original data, data consistency (DC) processing is performed on the reconstruction results after each step of the PC sampler. According to (4), the minimization problem is succinctly described as follows:

$$\min_x \{ \|P(m)x - y\|_2^2 + \lambda \|x - x_\tau\|_2^2 \}, \quad (18)$$

where  $x_\tau$  represents the sinogram projection data generated by the network, while  $x$  also denotes the sinogram projection data to be reconstructed. Therefore, the corresponding solutions can be derived through the application of first-order optimality conditions:

$$x^*(v) = \begin{cases} x_\tau(v), & \text{if } v \notin \Omega \\ \frac{[P^T(m)y(v) + \lambda x_\tau(v)]}{1 + \lambda}, & \text{if } v \in \Omega \end{cases} \quad (19)$$

where  $\Omega$  is represented by specific locations sampled within the projection domain.  $x_\tau(v)$  represents the entry at index  $v$  in projection domain generated by the network. Furthermore, a detailed operational guide for the training and inference stages is provided by **Algorithm 2**, ensuring the efficiency and accuracy of the entire reconstruction process.

---

#### Algorithm 2: MSDiff for Iterative Generation Process

---

- 1: Setting:**  $S_{\theta_1}, S_{\theta_2}, T, \sigma, \varepsilon$
  - 2: Initial data:**  $x = K(U)$
  - 3:**  $\{x^T\} \sim \mathcal{N}(0, \sigma_{max}^2 \mathbf{I})$
  - 4: For**  $i, j = T - 1$  **to** 0 **do**
  - 5:**  $x'_{i,j} = x_{i,j} \cdot \text{mask}_1, x^*_{i,j} = (1 - \text{mask}_1) \odot x_{i,j}$
  - 6:** Update  $x'_{i-1,j} \leftarrow \text{Predictor}(x'_{i,j}, \sigma_i, \sigma_{i+1}, S_{\theta_2})$
  - 7:** Update  $x'_{i-1,j}$  via (19)
  - 8:** Update  $x'_{i-1,j} \leftarrow \text{Corrector}(x'_{i-1,j}, \sigma_i, \varepsilon_i, S_{\theta_2})$
  - 9:** Update  $x'_{i-1,j}$  via (19)
  - 10:**  $x_{i-1,j} = x'_{i-1,j} + x^*_{i,j}$
  - 11:** Update  $x_{i-1,j-1} \leftarrow \text{Predictor}(x_{i-1,j}, \sigma_i, \sigma_{i+1}, S_{\theta_1})$
  - 12:** Update  $x_{i-1,j-1}$  via (19)
  - 13:** Update  $x_{i-1,j-1} \leftarrow \text{Corrector}(x_{i-1,j-1}, \sigma_i, \varepsilon_i, S_{\theta_1})$
  - 14:** Update  $x_{i-1,j-1}$  via (19)
  - 15: End for**
  - 16:** Obtain the final result by (15)
  - 17: Return**  $\bar{I}$
- 

In summary, the MSDiff processes images by considering various levels of detail and structure, from coarse to fine, simulating a transition from large-scale (global features) to small-scale (local details). The model analyzes and processes images across multiple dimensional layers, enhancing local features while maintaining global consistency. To validate the effectiveness of the proposed multi-scale diffusion model reconstruction strategy, a single FDM is also constructed as a comparative method. This baseline model is trained solely on complete sinogram data, with its reconstruction process including only a single iteration using the FDM. Specific quantitative evaluation metrics and comparison results are provided in the experimental section.

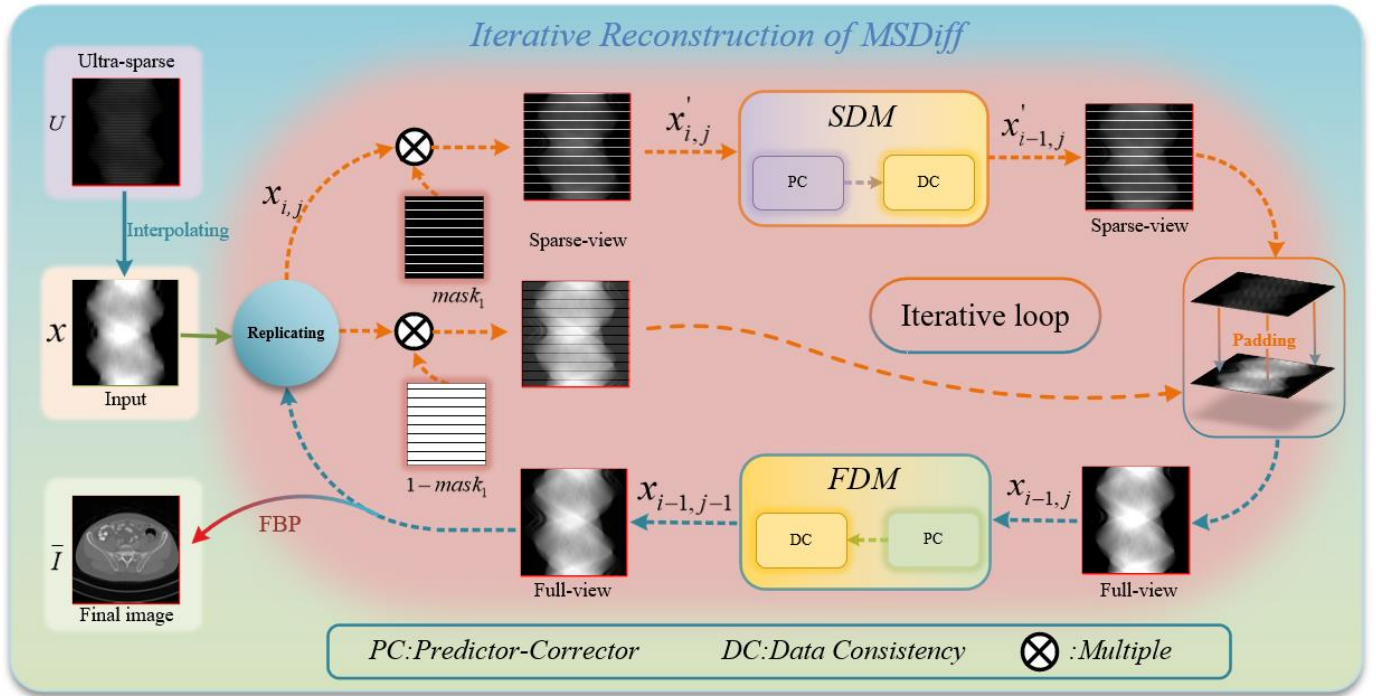


Fig. 4. Pipeline of the ultra-sparse view reconstruction procedure in MSDiff. Ultra-sparse view reconstruction is conducted in an iterative manner.

#### IV. EXPERIMENTS

##### A. Data Specification

**AAPM Challenge Data:** In this study, simulated abdominal imaging data from the 2016 AAPM CT Low Dose Grand Challenge, provided by Mayo Clinic, are initially utilized. A total of 5338 normal-dose CT images with a resolution of  $512 \times 512$  and a thickness of 1mm are selected and divided into training, validation, and testing sets, with 4742 slices designated for training, 584 for validation, and 12 for testing. Projection data are simulated by adding Poisson noise to the sinograms generated from the normal-dose images to create artifact-free images. Artifact-free images are obtained using the FBP algorithm with 720 projection angles, serving as the standard reference. Subsets of 10, 20, and 30 views are extracted from the full sinogram to evaluate the multi-scale diffusion model algorithm for ultra-sparse view CT reconstruction. For fan-beam CT reconstruction, sinograms are generated using Siddon's ray-driven algorithm. The distances from the rotation center to the source and to the detector are both set at 400. The detector, composed of 720 elements each with a width of 413, features a total of 720 projection views evenly distributed.

**CIRS Phantom Data:** A high-quality CT volume dataset measuring  $512 \times 512 \times 100$  voxels, with each voxel size at  $0.78 \times 0.78 \times 0.625$ , is acquired exclusively for testing purposes. This dataset is obtained using a humanoid CIRS phantom on the GE Discovery HD750 CT system, with a tube current set to 600 milliamperere-seconds. The distance of source-to-axis is recorded as 573, and the distance of source-to-detector as 1010. Full projection data from 720 views are collected, from which subsets of 10, 20, and 30 views are extracted for algorithm performance evaluation. To further validate the robustness of the proposed method, prior knowledge acquired from the AAPM Challenge data is used to assess its performance on the CIRS Phantom da-

taset. Additionally, two score-based networks trained on the AAPM data are employed to verify its generalization ability.

**Preclinical Mouse Data:** To validate the effectiveness of the proposed MSDiff in preclinical micro-CT applications, the networks trained on AAPM challenge data within MSDiff are transferred to preclinical mouse data. Deceased mouse is scanned using an industrial CT system equipped with a microfocus X-ray source and a flat-panel X-ray detector. While the specifications of the X-ray source in industrial CT systems are primarily designed for non-destructive testing of materials, they may not be optimally suited for preclinical mouse studies. However, this mismatch does not affect the evaluation of MSDiff for ultra-sparse view CT reconstruction. The distance from the source to the detector and the object are 1150 and 950, respectively. The detector consists of  $1024 \times 1024$  pixels, each detector unit measuring  $0.2 \times 0.2$ . Projections consisting of 500 views are distributed within the angular range. The reconstructed image forms a matrix of size  $512 \times 512$ , with each pixel measuring  $0.15 \times 0.15$ . With 500 views distributed within the angular range, 25 views are obtained across the scanning range when the subsampling factor is set to 20.

##### B. Model Training and Parameter Selection

In the experiments, the FDM and SDM models are trained using the Adam optimization algorithm, as the training process of VE-SDE proposed by Song *et al.* [40]. Specifically, an initial learning rate of  $10^{-4}$  is set, with a warm-up phase consisting of 5000 steps and gradient clipping established at 1. The weights are initialized using the Kaiming initialization method. The implementation code is composed in Python, utilizing the Operator Discretization Library (ODL) [48] and PyTorch. Computational tasks are carried out on a workstation equipped with a GPU (NVIDIA GTX 1080Ti-11GB).

In the proposed multi-scale model architecture, the full-sampling model is trained exclusively on complete sine curve data to accurately reconstruct images. Conversely, the under-sampling model is trained on sparse sine curve data corresponding to the original CT images, enabling it to learn the capability to reconstruct images from sparse data.

During the image inference phase, the number of external loop iterations is set to 1450. In the internal prediction and correction processes, the decayed Langevin dynamics are employed to better sample and explore the solution space at each execution step. To quantitatively evaluate and compare the reconstruction results, three standard metrics are employed, including Peak Signal-to-Noise Ratio (PSNR), Structural Similarity Index (SSIM) [49], and Mean Squared Error (MSE) [50]. Higher PSNR and SSIM values or lower MSE values are indicative of better reconstruction quality. For those interested in exploring our method, the source code is publicly accessible at: <https://github.com/yqx7150/MSDiff>.

### C. Fan-beam CT Reconstruction

In this section, fan-beam ultra-sparse view CT reconstruction is applied using the AAPM Challenge data, CIRS phantom data, and preclinical mouse dataset, with 10, 20, and 30 projection views employed for comparison. Furthermore, to validate the performance of MSDiff, it is compared with other reconstruction methods, including FBP [51], U-Net [16], FBPCConvNet [52], and GMSD [27]. FBP, a classic technique, is widely used in CT image reconstruction and is commonly employed for sparse-view CT reconstruction tasks. U-Net and FBPCConvNet, both supervised deep reconstruction methods, are utilized wherein U-Net is recognized as a neural network architecture for interpolating single-slice images from sparse sampling, followed by CT image reconstruction using the FBP algorithm. FBPCConvNet is a combination of FBP with deep learning techniques to enhance CT reconstruction effects, while GMSD is known as an unsupervised deep reconstruction method capable of generating high-quality images.

Tables I-II present the quantitative results reconstructed from 10, 20, and 30 views, where the best PSNR, SSIM, and MSE values for images reconstructed from different projection views are highlighted in bold. Visual results are shown in Figs. 5-8.

**AAPM Challenge Data Study:** In the experiments of ultra-sparse view CT reconstruction using 10, 20, and 30 views, a comprehensive evaluation of the reconstruction results is conducted on the AAPM Challenge dataset, with the average PSNR, SSIM, and MSE values summarized in Table I. The results demonstrate that the proposed MSDiff method surpasses other reconstruction techniques across these evaluation metrics. Particularly, MSDiff exhibits significant advantages in improving image quality compared to existing technologies.

MSDiff is prominently recognized for its enhancement of PSNR compared to the FBP technique. Furthermore, the visual performance of MSDiff aligns well with its outstanding quantitative evaluation metrics. As demonstrated in Figs. 5 and 6, with the increase in the number of projection views, a significant improvement in image quality reconstructed by MSDiff is observed, whereas images reconstructed by FBP and U-Net methods are seen to possess lower quality due to the blurriness of key details and structures. Specifically, the shortcomings in recovering complex details by FBPCConvNet and the edge blurriness by GMSD are elaborated. In contrast, images produced by MSDiff are not only rich in detail but also accurately depict contour information, showcasing its superior capabilities in detail recovery and structure representation.

As shown in Fig. 6, a leading position in providing finesse in detail and structural information is consistently maintained by MSDiff, exhibiting superior visual effects compared to other methods. This validates not only does MSDiff outperform other methods in quantitative evaluation, but also holds a significant advantage in visual effects. Compared to GMSD, which primarily focuses on learning the overall characteristics of sine curves, further refinement in detail processing is achieved by MSDiff by integrating SDM, resulting in more accurate and comprehensive reconstruction. This approach enables MSDiff to capture richer feature information, thereby reconstructing complete and clear image contours.

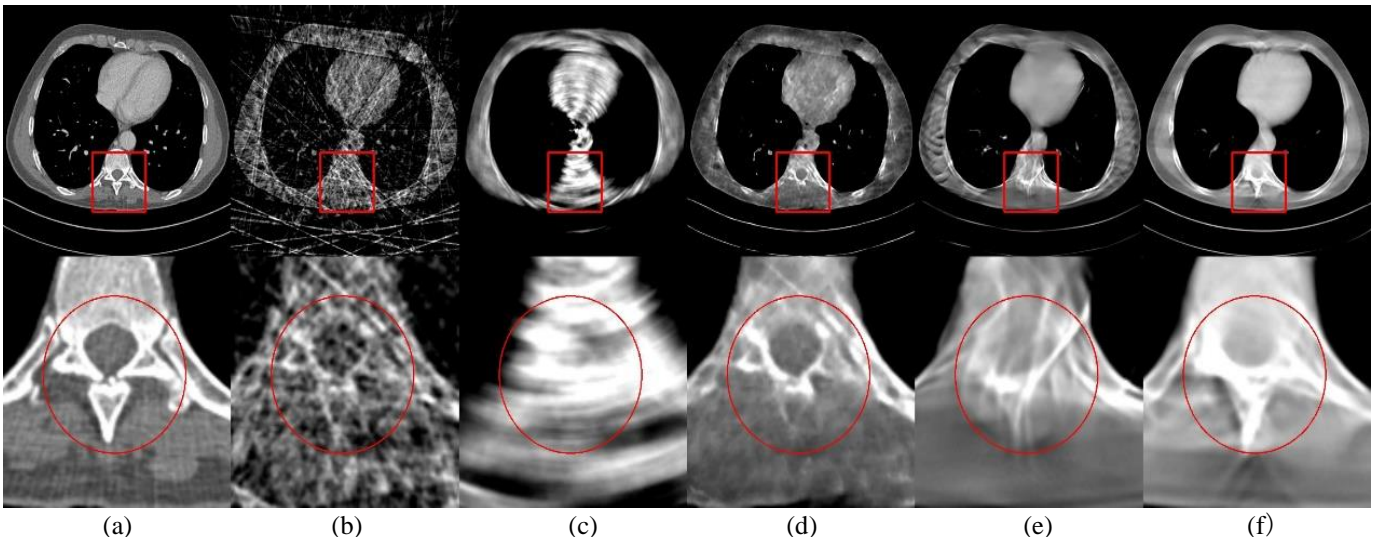


**Fig. 5.** Reconstruction of images with 20 views using different methods. (a) The GT versus the images reconstructed by (b) FBP, (c) U-Net, (d) FBPCConvNet, (e) GMSD, and (f) MSDiff. Display windows are all set to [-80, 80] HU. The second row shows the extracted ROI.

Table I  
RECONSTRUCTION PSNR/SSIM/MSE( $10^{-3}$ ) OF AAPM CHALLENGE DATA USING DIFFERENT METHODS AT 10, 20 AND 30 VIEWS.

Views	FBP	U-Net	FBPConvNet	GMSD	MSDiff
10	14.52/0.3404/35.9	16.69/0.6819/24.7	23.64/ <b>0.8559</b> /5.3	23.13/0.7869/5.0	<b>23.96</b> /0.8092/ <b>4.5</b>
20	17.81/0.4018/16.9	19.31/0.7220/12.5	26.82/0.9011/3.4	26.79/0.8614/2.2	<b>29.02</b> / <b>0.9028</b> / <b>1.3</b>
30	19.52/0.4636/11.5	20.23/0.8244/10.3	29.68/0.9197/1.1	29.63/0.9102/1.1	<b>32.48</b> / <b>0.9504</b> / <b>0.6</b>

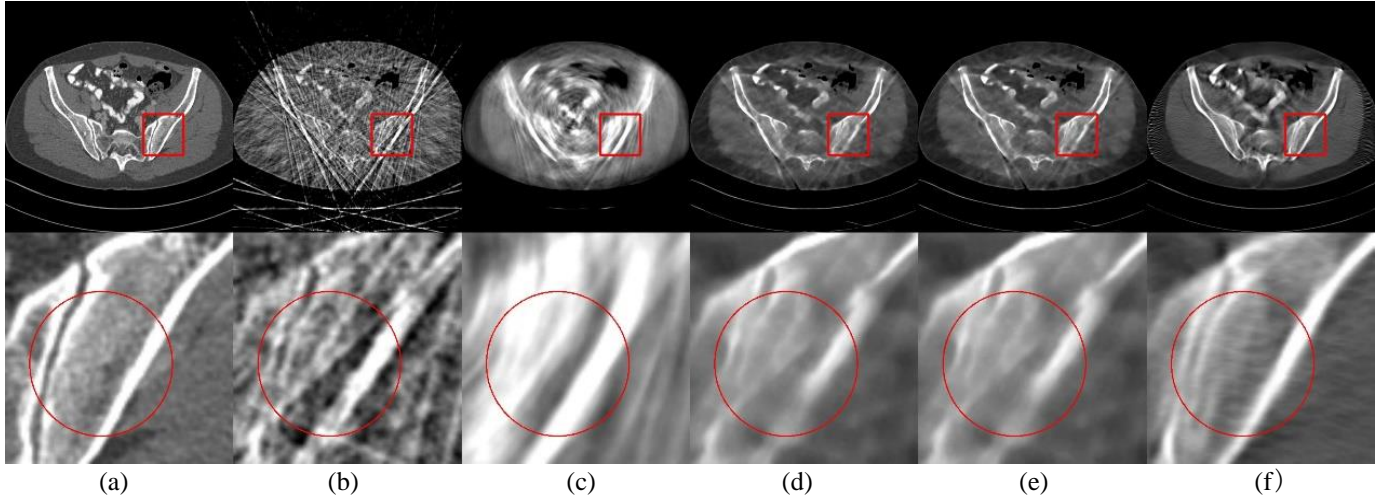


Fig. 6. Reconstruction of images with 30 views using different methods. (a) The GT versus the images reconstructed by (b) FBP, (c) U-Net, (d) FBPConvNet, (e) GMSD, and (f) MSDiff. Display windows are all set to [-170, 250] HU. The second row shows the extracted ROI.

#### D. Generalization Test

**CIRS Phantom Data Study:** To validate the generalization performance, the model trained on the AAPM dataset is used to test the CIRS Phantom data. Table II presents the quantitative results obtained from the CIRS Phantom data. Notably, the method is surpassed by other comparative methods in terms of the highest quantitative metrics. An important finding is that higher structural similarity on the CIRS Phantom dataset is exhibited by MSDiff. GMSD is outperformed by the MSDiff method. Compared to these methods, significant performance improvements across various metrics and evaluation criteria are demonstrated by MSDiff. Specifically, higher accuracy, stronger detail preservation capability, and clearer image reconstruction ability are consistently maintained by MSDiff. This robust performance highlights the effectiveness of MSDiff in surpassing GMSD.

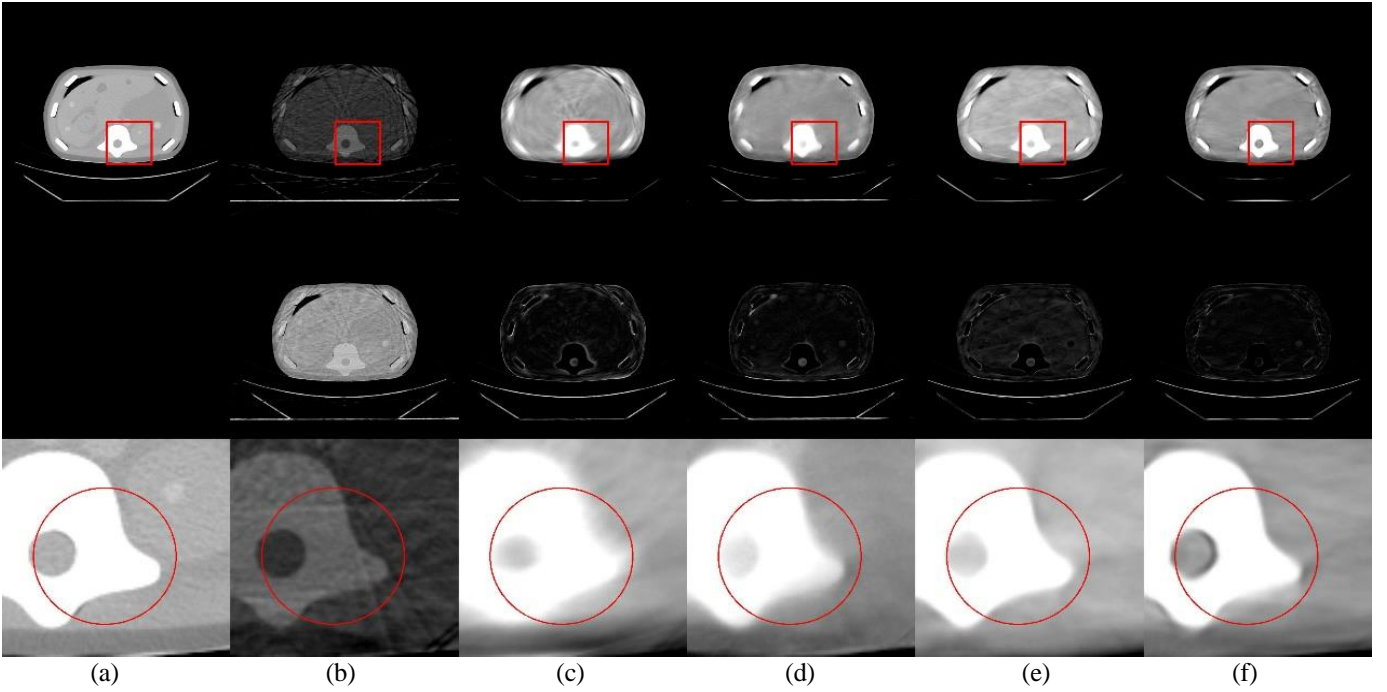
Moreover, exceptional visual performance is exhibited by MSDiff. In Figs. 7 and 8, the enlarged regions of interest are highlighted with red rectangles. Under 20 and 30 viewing angles, significant streak artifacts, compared to FBP, are reduced by unsupervised U-Net and FBPConvNet (combining FBP and deep learning). Conversely, blurred contours and unclear details are exhibited, resulting in poor visual outcomes. Additionally, while a notable improvement in reducing artifacts is shown by GMSD, some texture information is also sacrificed. In contrast, outstanding reconstruction capabilities are demonstrated by the MSDiff method, effectively reducing artifacts in ultra-sparse view CT and restoring image detail information. Compared to other similar reconstruction methods, textures and details are excellently preserved by MSDiff, offering optimal visual effects.

Table II  
RECONSTRUCTION PSNR/SSIM/MSE( $10^{-3}$ ) OF CIRS PHANTOM DATA USING DIFFERENT METHODS AT 10, 20, AND 30 VIEWS.

Views	FBP	U-Net	FBPConvNet	GMSD	MSDiff
10	12.02/0.2846/62.8	19.99/0.7293/10.0	20.67/0.7566/8.7	20.83/ <b>0.7877</b> /8.3	<b>21.72</b> /0.7745/ <b>6.8</b>
20	12.71/0.3312/53.7	21.75/0.7995/6.7	21.89/0.7962/6.5	23.29/0.8616/4.7	<b>24.86</b> / <b>0.8808</b> / <b>3.3</b>
30	12.77/0.4159/52.8	25.76/0.8786/2.7	24.43/0.8193/3.7	26.67/0.9053/2.2	<b>26.82</b> / <b>0.9243</b> / <b>2.1</b>

**Preclinical Mouse Reconstruction Results:** To evaluate efficiency on real data, the network within MSDiff is trained on AAPM Challenge Data and tested on preclinical mouse data. Fig. 8 visualizes and presents the reconstructed images using different methods. The reference reconstruction is originated from full-projection data. Notably, Fig. 8 vividly displays the streaking artifacts that are present in FBP reconstruction. Upon examining the extracted regions of interest (ROIs), it is observed that both U-Net and FBPConvNet tend to produce blurred structures,

which affect the clarity of details within the ROIs. The results in image structures deviating from the original images, indicating a significant deficiency in preserving complex structures. In contrast, the reconstructed results of GMSD show the general image structure. Compared to GMSD, approximate edges are displayed by MSDiff, with image structures being closer to the GT. Table III provides a detailed quantitative analysis of the clinical mouse data, highlighting the improvements of MSDiff over GMSD across various metrics.



**Fig. 7.** Reconstruction of images with 30 views using different methods. (a) The GT versus the images reconstructed by (b) FBP, (c) U-Net, (d) FBPCConvNet, (e) GMSD, and (f) MSDiff. Display windows are all set to  $[-80, 80]$  HU. The second row shows the difference images, and the third row displays the extracted ROI.

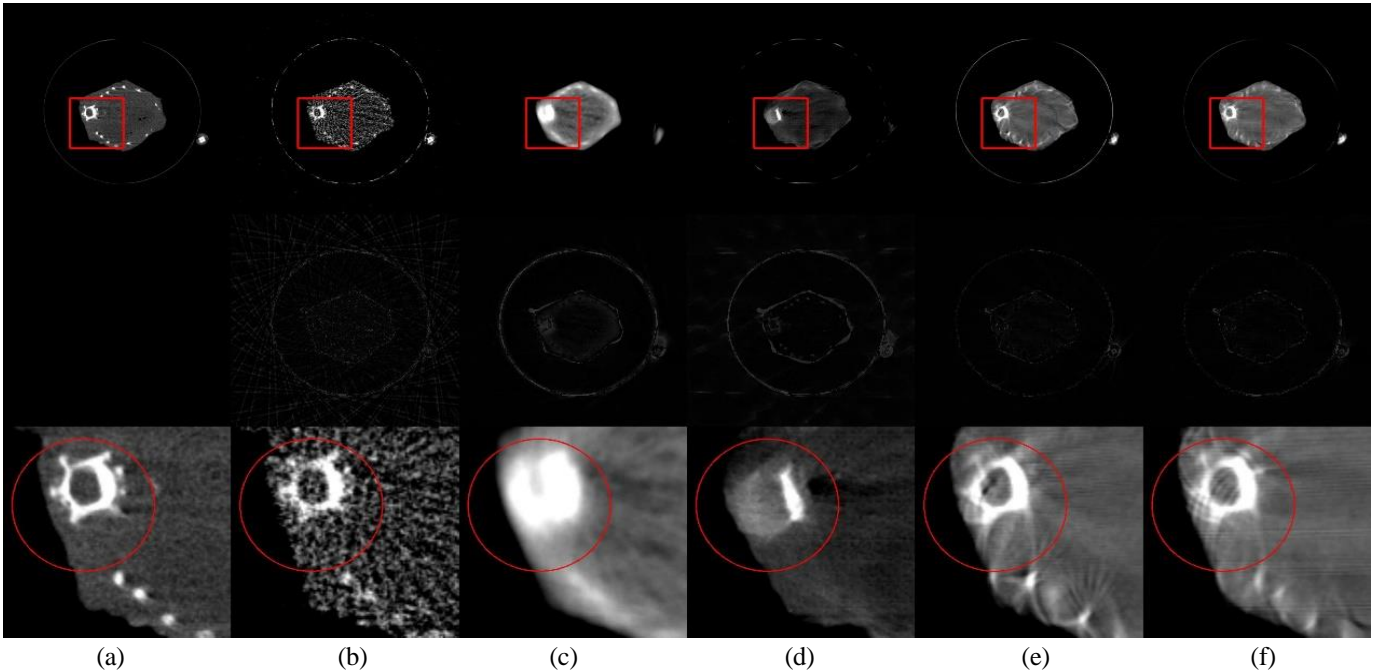


**Fig. 8.** Reconstruction images from 25 views using different methods. (a) The GT versus the images reconstructed by (b) FBP, (c) U-Net, (d) FBPCConvNet, (e) GMSD, and (f) MSDiff. Display windows are all set to  $[-250, 220]$  HU. The second row shows the difference images.

Table III  
RECONSTRUCTION PSNR/SSIM/MSE( $10^{-3}$ ) OF PRECLINICAL MOUSE DATA  
USING DIFFERENT METHODS AT 25 VIEWS.

Methods	PSNR	SSIM	MSE( $10^{-3}$ )
FBP	24.25	0.5105	3.76
U-Net	28.14	0.8474	1.54
FBPCConvNet	26.23	0.6110	2.38
GMSD	33.28	0.9200	0.47
MSDiff	<b>34.04</b>	<b>0.9204</b>	<b>0.40</b>

### E. Profile Lines Analysis

In this section, the profile lines of reconstructed results obtained by different methods are compared to evaluate their edge-preserving performance. As shown in Fig. 9, the profile lines generated by FBP, U-Net, and FBPCConvNet do not match well with the profile lines of the ground truth. Meanwhile, the profile lines produced by GMSD and MSDiff are found to be closer to the ground truth, demonstrating the strong profile-preserving capability of diffusion models. In a comprehensive comparison, the most accurate profile lines are

generated by MSDiff. Additionally, it is observed that the image profile lines produced in areas with significant gray-scale changes are noticeably different. The limited availability of anatomical information on CT images could be a possible reason for this discrepancy. Despite these challenges, Fig.9 shows a significant agreement between the image profile lines generated by this method and the ground truth data, indicating the robust profile-preserving capability of MSDiff.

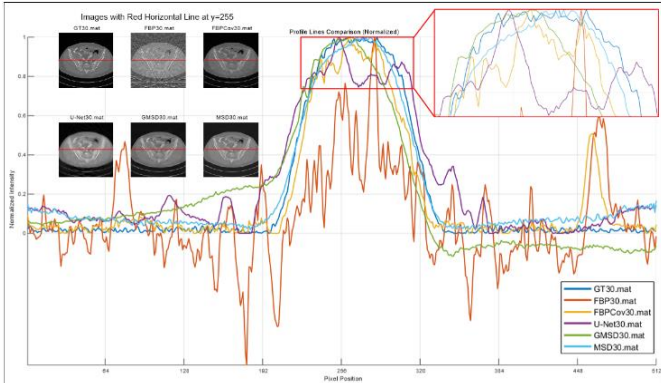


**Fig. 9.** Comparison of CT image profiles between ground truth and other methods on abdomen images. Red lines represent the location where the line profile is measured.

#### F. Ablation Study

This work introduces a MSDiff strategy that integrates the strengths of both the FDM and the SDM, focusing on capturing global coherence and precise local details of images. Through detailed ablation experiments, the specific impacts of FDM and SDM on image reconstruction outcomes are explored. As demonstrated in Table IV, a significant advantage in enhancing image reconstruction performance through the use of the multi-scale diffusion model is shown. The combination of FDM and SDM not only preserves the individual strengths of each model but also leads to noticeable improvements in the quality of reconstructions.

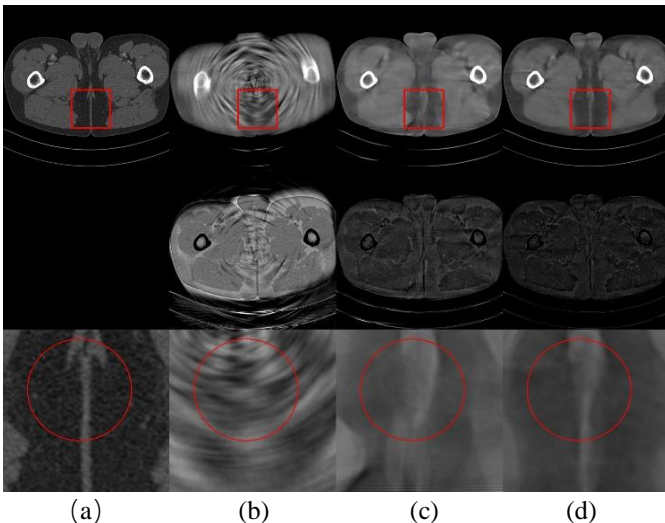


**Fig. 10.** Reconstructed images from 30 different perspectives obtained using different methods: (a) GT, (b) MSDiff without the FDM module, (c) MSDiff without the SDM module, and (d) fully implemented MSDiff. Display windows are all set to  $[-180, 250]$  HU. The second and third rows depict difference images and extracted ROI.

To further elucidate the effects brought by the integration of models, qualitative analysis results in Fig. 10 reveal the clear distinction between employing and not employing the SDM module within the MSDiff model. Versions without the integrated FDM module display disorganized image structures and a lack of detailed features. Conversely, the MSDiff model lacking the SDM component is shown to perform poorly in reproducing the global outlines of images, primarily due to the absence of a refinement process for enhancing fine structures and textures. This shortcoming becomes particularly evident in differential images, highlighting the challenges of restoring the complete image framework relying solely on local information. Through the effective integration of FDM and SDM, the MSDiff model not only optimizes the details and global information in image reconstructions but also demonstrates its strong capability for comprehensive reconstruction using complementary strategies.

Table IV  
RECONSTRUCTION RESULTS ON AAPM CHALLENGE DATA

Methods	Views	PSNR	SSIM	MSE( $10^{-3}$ )
FDM	10	22.06	0.6877	6.4
	20	26.36	0.8297	2.5
	30	29.85	0.9199	1.1
SDM	10	17.74	0.6769	19.1
	20	19.96	0.7459	10.9
	30	21.38	0.7710	7.6
MSDiff	<b>10</b>	<b>23.96</b>	<b>0.8092</b>	<b>4.5</b>
	<b>20</b>	<b>29.02</b>	<b>0.9028</b>	<b>1.3</b>
	<b>30</b>	<b>32.48</b>	<b>0.9504</b>	<b>0.6</b>

#### V. DISCUSSION

In the field of sparse-view and limited-angle CT imaging, the precise reconstruction of complex textures and structures poses a significant challenge. To validate the enhancement effects of sparse-view models on the quality of image reconstruction, projection data sampled using masks of 60, 90, 120, and 180 views are utilized. Subsequently, networks are trained sequentially to ascertain the distributions of different sparse projection data. Table V displays the average test results on the AAPM validation set for different sparse-view models. After being reconstructed by different sparse-view models, it can be concluded from the data in the table that ultra-sparse views, show varying degrees of improvement. Our research results further validate that the sequential fusion of FDM and SDM modules significantly enhances the precision and detail representation in CT reconstruction.

Table V  
RECONSTRUCTION RESULTS ON AAPM CHALLENGE DATA

View Mask	10	15	30
None	23.15/0.7860/5.0	25.32/0.8327/3.0	29.65/0.9100/1.21
60	22.32/0.6938/6.1	25.35/0.8177/3.1	<b>30.66/0.9301/0.93</b>
90	<b>24.85/0.8436/3.4</b>	<b>28.64/0.9083/1.4</b>	<b>32.80/0.9474/0.78</b>
120	<b>23.96/0.8092/4.5</b>	<b>26.97/0.8790/2.3</b>	<b>32.45/0.9495/0.64</b>
180	22.41/0.7556/6.6	<b>26.47/0.8643/2.7</b>	<b>31.64/0.9411/0.78</b>

Moreover, considering the scarcity of medical imaging data, the dependency on large datasets for model training presents a significant challenge. To address this issue, future efforts will explore imaging techniques based on limited or single data samples. Despite the limited data volume, profound insights may still be produced. Additionally, it has been recognized that fine-tuning parameters, such as learning rate adjustments, gradient clipping, and learning rate warm-up, play a crucial role in ensuring model stability, convergence, and high-performance output. Subsequent research will further optimize these parameters to enhance the efficiency and accuracy of the model.

## VI. CONCLUSIONS

Despite the significant advancements achieved by deep learning techniques in the field of CT image reconstruction, the challenge of reconstructing ultra-sparse CT views persisted. Addressing this issue, a novel approach for ultra-sparse view CT image reconstruction, termed as MSDiff, was introduced in this study. This involved simultaneously training score networks under both fully sampled and under-sampled conditions, ingeniously capturing image priors across different scales. The precision of image reconstruction was substantially enhanced through an iterative update mechanism that alternated between the utilization of both networks for image prediction and fidelity enhancement. Moreover, the performance of the model was further refined with the incorporation of diverse sparse model combinations and the introduction of perception-based loss functions. Tested across two public datasets, the MSDiff approach was demonstrated to surpass existing single-network models in both quantitative assessments and visual outcomes, offering an effective strategy for reducing radiation dosage in CT imaging. Although MSDiff, as a projection domain solution, might have exhibited image blurring and smoothing in high-contrast regions, future work planned to overcome this limitation by assimilating priors from the image domain. Overall, this research validated the effectiveness of using an iterative approach with multiple diffusion models for medical image reconstruction, presenting a feasible pathway for ultra-sparse reconstruction techniques.

## REFERENCES

- [1] G. N. Hounsfield, "Computed medical imaging," *Science*, vol. 210, no. 4465, pp. 22-28, Oct. 1980.
- [2] M. Lell and M. Kachelrieß, "Computed Tomography 2.0: New detector technology, AI, and other developments," *Investigative Radiology*, vol. 58, no. 8, pp. 587-601, Aug. 2023.
- [3] D. J. Brenner and E. J. Hall, "Computed tomography—an increasing source of radiation exposure," *New Engl. J. Med.*, vol. 357, no. 22, pp. 2277-2284, 2007.
- [4] D. Bos, N. Guberina, S. Zensen, M. Opitz, M. Forsting, and A. Wetter, "Radiation exposure in computed tomography," *Dtsch Arztebl Int.*, vol. 120, no. 9, pp. 135-141, Mar. 2023.
- [5] Z. Shu and A. Entezari, "Sparse-view and limited-angle CT reconstruction with untrained networks and deep image prior," *Comput. Methods Programs Biomed.*, vol. 226, pp. 107167, Nov. 2022.
- [6] I. Ayad, C. Tarpau, J. Cebeiro, and M. K. Nguyen, "Tomographic reconstruction from sparse-view and limited-angle data using a generative adversarial network," in *Proc. 16th Int. Conf. Signal-Image Technol. & Internet-Based Syst. (SITIS)*, pp. 341-347, Dec. 2022.
- [7] E. Xie, P. Ni, R. Zhang, and X. Li, "Limited-Angle CT Reconstruction with generative adversarial network sinogram inpainting and unsupervised artifact removal," *Applied Sciences*, vol. 12, no. 12, pp. 6268, Dec. 2022.
- [8] L. Zhang, H. Liang, X. Hu, and Y. Xu, "A regularized limited-angle CT reconstruction model based on sparse multi-level information groups of the images," in *Image and Graphics Technologies and Applications*, pp. 267-282, Springer, 2021.
- [9] S. Niu, Y. Bian Z, et al., "Sparse-view x-ray CT reconstruction via total generalized variation regularization," *Phys. Med. Biol.*, vol. 59, no. 12, pp. 2997-3017, Jun. 2014.
- [10] G. Wang, J. C. Ye, K. Mueller, and J. A. Fessler, "Image reconstruction is a new frontier of machine learning," *IEEE Trans. Med. Imag.*, vol. 37, no. 6, pp. 1289-1296, 2018.
- [11] E. Y. Sidky, C. M. Kao, and X. Pan, "Accurate image reconstruction from few-views and limited-angle data in divergent-beam CT," *J. X-ray Sci. Technol.*, vol. 14, no. 2, pp. 119-139, 2006.
- [12] D. L. Donoho, "Compressed sensing," *IEEE Trans. Inf. Theory*, vol. 52, no. 4, pp. 1289-1306, Apr. 2006.
- [13] Z. Chen, X. Jin, L. Li, and G. Wang, "A limited-angle CT reconstruction method based on anisotropic TV minimization," *Phys. Med. Biol.*, vol. 58, no. 7, pp. 2119, Apr. 2013.
- [14] Y. Xi, P. Zhou, H. Yu, et al., "Adaptive-weighted high order TV algorithm for sparse-view CT reconstruction," *Medical Physics*, vol. 50, no. 9, pp. 5568-5584, Sep. 2023.
- [15] C. Ma, Z. Li, J. Zhang, Y. Zhang, and H. Shan, "FreeSeed: Frequency-band-aware and self-guided network for sparse-view CT reconstruction," in *International Conference on Medical Image Computing and Computer-Assisted Intervention*, pp. 250-259, 2023.
- [16] H. Lee, J. Lee, H. Kim, B. Cho, and S. Cho, "Deep-neural-network-based sinogram synthesis for sparse-view CT image reconstruction," *IEEE Trans. Radiat. Plasma Med. Sci.*, vol. 3, no. 2, pp. 109-119, Mar. 2019.
- [17] Y. Zhang, D. Hu, S. Hao, et al., "DREAM-Net: Deep residual error iterative minimization network for sparse-view CT reconstruction," *IEEE Journal of Biomedical and Health Informatics*, vol. 27, no. 1, pp. 480-491, Jan. 2022.
- [18] A. Neroladaki, D. Botsikas, S. Boudabbous, C. D. Becker, and X. Montet, "Computed tomography of the chest with model-based iterative reconstruction using a radiation exposure similar to chest X-ray examination: preliminary observations," *Eur. Radiol.*, vol. 23, pp. 360-366, Feb. 2013.
- [19] G. H. Chen, J. Tang, and S. Leng, "Prior image constrained compressed sensing (PICCS): a method to accurately reconstruct dynamic CT images from highly undersampled projection data sets," *Med. Phys.*, vol. 35, no. 2, pp. 660-663, Feb. 2008.
- [20] M. S. Pearce, A. J. Salotti, P. M. Little, et al., "Radiation exposure from CT scans in childhood and subsequent risk of leukaemia and brain tumours: a retrospective cohort study," *The Lancet*, vol. 380, no. 9840, pp. 499-505, Aug. 2012.
- [21] D. J. Brenner et al., "Cancer risks attributable to low doses of ionizing radiation: assessing what we really know," *Proceedings of the National Academy of Sciences*, vol. 100, no. 24, pp. 13761-13766, Nov. 2003.
- [22] J. Bian, J. H. Siewerdsen, X. Han, et al., "Evaluation of sparse-view reconstruction from flat-panel-detector cone-beam CT," *Phys. Med. Biol.*, vol. 55, no. 22, pp. 6575, Nov. 2010.
- [23] W. R. Hendee and F. M. Edwards, "ALARA and an integrated approach to radiation protection," *Semin. Nucl. Med.*, vol. 16, no. 2, pp. 142-150, Apr. 1986.
- [24] W. Wu and Y. Wang, "Data-iterative optimization score model for stable ultra-sparse-view CT reconstruction," 2023, *arXiv preprint arXiv:2308.14437*.
- [25] Y. Chan, X. Liu, T. Wang, et al., "An attention-based deep convolutional neural network for ultra-sparse-view CT reconstruction," *Computers in Biology and Medicine*, vol. 161, pp. 106888, Apr. 2023.
- [26] C. Saharia, J. Ho, W. Chan, et al., "Image super-resolution via iterative refinement," *IEEE transactions on pattern analysis and machine intelligence*, vol. 45, no. 4, pp. 4713-4726, Apr. 2022.
- [27] B. Guan, C. Yang, L. Zhang, S. Niu, M. Zhang, and Q. Liu, "Generative modeling in sinogram domain for sparse-view CT reconstruction," *IEEE Trans. Radiat. Plasma Med. Sci.*, vol. 8, pp. 195-207, Feb. 2024.
- [28] K. Xu, S. Lu, B. Huang, W. Wu, and Q. Liu, "Stage-by-stage wavelet optimization refinement diffusion model for sparse-view CT reconstruction," *IEEE Transactions on Radiation and Plasma Medical Sciences*, 2024.

- [29] M. T. McCann, H. Chung, J. C. Ye, and M. L. Klasky, "Score-based diffusion models for bayesian image reconstruction," in *Proc. IEEE Int. Conf. Image Process. (ICIP), IEEE*, pp. 111-115, 2023.
- [30] W. Xia, C. Niu, W. Cong, and G. Wang, "Sub-volume-based denoising diffusion probabilistic model for cone-beam CT reconstruction from incomplete data," *arXiv preprint arXiv:2303.12861*, Mar. 2023.
- [31] W. Xia, W. Cong, and G. Wang, "Patch-based denoising diffusion probabilistic model for sparse-view CT reconstruction," *arXiv preprint arXiv:2211.10388*, 2022.
- [32] X. Li, K. Shang, G. Wang, and M. D. Butala, "Ddmm-synth: A denoising diffusion model for cross-modal medical image synthesis with sparse-view measurement embedding," *arXiv preprint arXiv:2303.15770*, 2023.
- [33] B. Huang, L. Zhang, S. Lu, B. Lin, W. Wu, and Q. Liu, "One sample diffusion model in projection domain for low-dose CT imaging," Nov. 2022, *arXiv preprint arXiv:2212.03630*.
- [34] L. Yang, Z. Zhang, Y. Song, et al., "Diffusion models: A comprehensive survey of methods and applications," *ACM Computing Surveys*, vol. 56, no. 4, pp. 1-39, Apr.-Jun. 2023.
- [35] F.-A. Croitoru, V. Hondru, R. T. Ionescu, and M. Shah, "Diffusion models in vision: A survey," *IEEE Trans. Pattern Anal. Mach. Intell.*, 2023.
- [36] J. Sohl-Dickstein, E. Weiss, N. Maheswaranathan, and S. Ganguli, "Deep unsupervised learning using nonequilibrium thermodynamics," in *Proc. Int. Conf. Mach. Learn., PMLR*, pp. 2256-2265, 2015.
- [37] J. Ho, A. Jain, and P. Abbeel, "Denoising diffusion probabilistic models," in *Adv. Neural Inf. Process. Syst.*, vol. 33, pp. 6840-6851, Dec. 2020.
- [38] Y. Song, J. Sohl-Dickstein, D. P. Kingma, A. Kumar, S. Ermon and B. Poole, "Score-based generative modeling through stochastic differential equations", *Proceedings of the International Conference on Learning Representations (ICLR 2021)*, pp. 1-36, 2021.
- [39] A. Q. Nichol and P. Dhariwal, "Improved denoising diffusion probabilistic models," in *Proc. Int. Conf. Mach. Learn., PMLR*, pp. 8162-8171, 2021.
- [40] Y. Song, J. Sohl-Dickstein, D. P. Kingma, A. Kumar, S. Ermon, and B. Poole, "Score-based generative modeling through stochastic differential equations," *arXiv preprint arXiv:2011.13456*.
- [41] Y. Song and S. Ermon, "Improved techniques for training score-based generative models," in: *Advances in Neural Information Processing Systems*, vol. 33, pp. 12438-12448, 2020.
- [42] Z. Wang, H. Zheng, P. He, W. Chen, and M. Zhou, "Diffusion-gan: Training gans with diffusion," Apr. 2022, *arXiv preprint arXiv:2206.02262*.
- [43] P. Dhariwal and A. Nichol, "Diffusion models beat gans on image synthesis," in *Adv. Neural Inf. Process. Syst.*, vol. 34, pp. 8780-8794, Dec. 2021.
- [44] Y. Song and S. Ermon, "Generative modeling by estimating gradients of the data distribution," in: *Advances in Neural Information Processing Systems*, vol. 32, 2019.
- [45] Low Dose CT Grand Challenge. Accessed: Apr. 6, 2017. [Online]. Available: <http://www.aapm.org/GrandChallenge/LowDoseCT/>.
- [46] C. McCollough, "TU-FG-207A-04: overview of the low dose CT grand challenge," *Med. Phys.*, vol. 43, no. 6Part35, pp. 3759-3760, Jun. 2016.
- [47] R. L. Siddon, "Fast calculation of the exact radiological path for a three-dimensional CT array," *Med. Phys.*, vol. 12, no. 2, pp. 252-255, Mar.-Apr. 1985.
- [48] J. Adler, H. Kohr, and O. Oktem, "Operator discretization library (ODL)," Software available from <https://github.com/odlgroup/odl>, vol. 5, 2017.
- [49] Z. Wang, A. C. Bovik, and E. P. Simoncelli, "Structural approaches to image quality assessment," in *Handbook of Image and Video Processing*, A. C. Bovik, Ed., 2nd ed., Academic Press, pp. 961-974, 2005.
- [50] Z. Wang, A. C. Bovik, H. R. Sheikh, and E. P. Simoncelli, "Image quality assessment: from error visibility to structural similarity," *IEEE Trans. Image Process.*, vol. 13, no. 4, pp. 600-612, Apr. 2004.
- [51] D. J. Brenner, C. D. Elliston, E. J. Hall, and W. E. Berdon, "Estimated risks of radiation-induced fatal cancer from pediatric CT," *Am. J. Roentgenol.*, vol. 176, no. 2, pp. 289-296, 2001.
- [52] K. H. Jin, M. T. McCann, E. Froustey, and M. Unser, "Deep convolutional neural network for inverse problems in imaging," *IEEE Trans. Image Process.*, vol. 26, no. 9, pp. 4509-4522, Sep. 2017.